remote sensing

MDPI

Article

Comparison of FNR and GNR Based on TROPOMI Satellite Data for Ozone Sensitivity Analysis in Chinese Urban Agglomerations

Jing Fan [1,2], Chao Yu [1,*], Yichen Li [1,2], Ying Zhang [1], Meng Fan [1], Jinhua Tao [1] and Liangfu Chen [1,2]

[1] State Key Laboratory of Remote Sensing and Digital Earth, Aerospace Information Research Institute, Chinese Academy of Sciences, Beijing 100101, China; fanjing23@mails.ucas.ac.cn (J.F.); liyichen211@mails.ucas.ac.cn (Y.L.); zhangying200907@aircas.ac.cn (Y.Z.); fanmeng@aircas.ac.cn (M.F.); taojh@aircas.ac.cn (J.T.); chenlf@aircas.ac.cn (L.C.)
[2] University of Chinese Academy of Sciences, Beijing 100049, China
* Correspondence: yuchao@aircas.ac.cn

Highlights

What are the main findings?

- Analyzed the spatiotemporal differences and causes of ozone sensitivity between FNR and GNR in four major urban agglomerations in China.
- Revealed a common spatial distribution pattern for both indices: VOC-limited regimes in urban centers and NO_x-limited regimes in suburban areas.

What is the implication of the main finding?

- Due to its higher sensitivity to anthropogenic VOCs, GNR classifications exhibit a stronger tendency toward NO_x-limited regimes compared to FNR.

Abstract

Currently, ozone (O_3) has become one of the primary air pollutants in China, underscoring the importance of analyzing ozone formation sensitivity (OFS) for effective pollution control. Ozone sensitivity indices serve as effective tools for OFS identification. Among them, the ratio of volatile organic compounds (VOCs) to nitrogen oxides (NO_x)—such as the formaldehyde-to-nitrogen dioxide ratio (FNR, defined as $HCHO/NO_2$, where HCHO represents VOCs and NO_2 represents NO_x)—is one of the most widely used satellite-based indicators. Recent studies have highlighted glyoxal (CHOCHO) as another critical ozone precursor, prompting the proposal of the glyoxal-to-nitrogen dioxide ratio (GNR, $CHOCHO/NO_2$) as an alternative metric. This study systematically compares the performance of FNR and GNR across four major urban agglomerations in China: Beijing–Tianjin–Hebei (BTH), the Yangtze River Delta (YRD), the Pearl River Delta (PRD), and the Chengdu–Chongqing (CY) region, by integrating satellite remote sensing with ground-based observations. Results reveal that both indices exhibit consistent spatial trends in OFS distribution, transitioning from VOC-limited regimes in urban centers to NO_x-limited regimes in surrounding suburban areas. However, differences emerge in threshold values and classification outcomes. During summer, FNR identifies urban areas as transitional regimes (or VOC-limited in regions such as YRD and PRD), while suburban areas are classified as NO_x-limited. In contrast, GNR, which shows heightened sensitive to anthropogenic VOCs (AVOCs), exhibits a more restricted spatial extent in the transition regimes. By autumn, most urban areas shift toward VOC-limited regimes, while suburban regions remain NO_x-limited. Thresholds for both VOCs and NO_x increase during this period, with GNR demonstrating stronger sensitivity to NO_x. These findings underscore that the choice

check for updates

Academic Editor: Manuel Antón

Received: 28 August 2025
Revised: 23 September 2025
Accepted: 25 September 2025
Published: 27 September 2025

Citation: Fan, J.; Yu, C.; Li, Y.; Zhang, Y.; Fan, M.; Tao, J.; Chen, L. Comparison of FNR and GNR Based on TROPOMI Satellite Data for Ozone Sensitivity Analysis in Chinese Urban Agglomerations. *Remote Sens.* **2025**, *17*, 3321. https://doi.org/10.3390/rs17193321

Copyright: © 2025 by the authors. Licensee MDPI, Basel, Switzerland. This article is an open access article distributed under the terms and conditions of the Creative Commons Attribution (CC BY) license (https://creativecommons.org/licenses/by/4.0/).

between FNR and GNR directly influences OFS determination, as their differing responses to biogenic and anthropogenic emissions lead to different conclusions. Future research should focus on integrating the complementary strengths of both indices to develop a more robust OFS identification method, thereby providing a theoretical basis for formulating effective ozone control strategies.

Keywords: ozone formation sensitivity; remote sensing; satellite; FNR; GNR

1. Introduction

Ground-level ozone (O_3), a major component of atmospheric pollution, significantly impacts human health, ecosystems, and climate change [1–3]. In the context of rapid urbanization and industrialization in China, O_3 pollution has become increasingly severe, emerging as the primary air pollutant affecting the country's air quality after $PM_{2.5}$ [4]. The frequent occurrence of urban O_3 pollution in China in recent years is fundamentally driven by high-intensity emissions of nitrogen oxides (NO_x) and volatile organic compounds (VOCs) [5]. The reaction of VOCs with hydroxyl radicals (OH) produces peroxyl radicals (RO_2), which compete with O_3 to oxidize NO to NO_2, thereby photolyzing and accelerating the net production of O_3 [6,7]. In this process, VOCs act as catalysts, leading to the formation of distinct O_3 production sensitivity regimes. Effective control of O_3 pollution requires accurately identifying its formation sensitivity to determine whether it is in VOC-limited, transition, or NO_x-limited regimes.

Traditionally, formaldehyde (HCHO) is used as a proxy for VOCs [8–10] and nitrogen dioxide (NO_2) as a proxy for NO_x [11], with their ratio, FNR ($HCHO/NO_2$), being used for ozone formation sensitivity (OFS) analysis [12–16]. Because FNR can be derived from satellite data, which offer excellent spatial coverage and timeliness, it has been widely applied in urban ozone sensitivity studies [17,18]. Research by Duncan et al. has shown that an FNR < 1 indicates a VOC-limited regime, while an FNR > 2 indicates a NO_x-limited regime [19,20]. The advantages of FNR include convenient data acquisition, simple calculation, and suitability for large-scale analysis. However, the sources of HCHO are complex, encompassing both biogenic [21,22] and anthropogenic contributions [23]. This complexity can lead to an underestimation of the role of anthropogenic VOCs (AVOCs), particularly in regions with high VOC levels [9]. To optimize the limitations of FNR, recent studies have proposed using glyoxal (CHOCHO) to represent VOCs and constructing the GNR ($CHOCHO/NO_2$) ratio [24,25]. CHOCHO is primarily derived from the secondary oxidation of anthropogenic sources, making it a more representative indicator of VOCs in urban environments and more sensitive to ozone formation [26–28]. Nevertheless, GNR also has its limitations. CHOCHO has a lower atmospheric abundance and limited data resources, and the accuracy of its satellite observation is significantly affected by instrument sensitivity and cloud interference [29].

Given the limitation of FNR affected by HCHO and the higher sensitivity of GNR to anthropogenic VOCs, it is crucial to compare the ozone formation sensitivity of these two indices under the same environmental conditions. In this study, we used data from the Tropospheric Monitoring Instrument (TROPOMI), which provides daily, global coverage, high-resolution satellite data, including column concentrations of HCHO, CHOCHO, and NO_2, providing reliable data support for FNR and GNR.

Based on TROPOMI satellite data and ground-based monitoring data, this study selects four major urban agglomerations in China—Beijing–Tianjin–Hebei (BTH), Yangtze River Delta (YRD), Pearl River Delta (PRD), and Chengdu–Chongqing (CY)—as its research

subjects. It compares the performance of FNR and GNR in ozone sensitivity classification, analyzes their spatiotemporal differences and the underlying reasons, and compares the classification results of both indicators with ground-based classification results.

2. Materials and Methods

2.1. Study Areas

The Beijing–Tianjin–Hebei (BTH), Yangtze River Delta (YRD), Pearl River Delta (PRD), and Chengdu–Chongqing (CY) regions are areas in China that experience severe O_3 pollution. Figure 1 illustrates the geographical locations of these four selected urban agglomerations. These regions are among the most economically developed, densely populated, and energy-intensive areas in the country. Each urban agglomeration has a unique industrial structure, emission source profile, and set of meteorological characteristics.

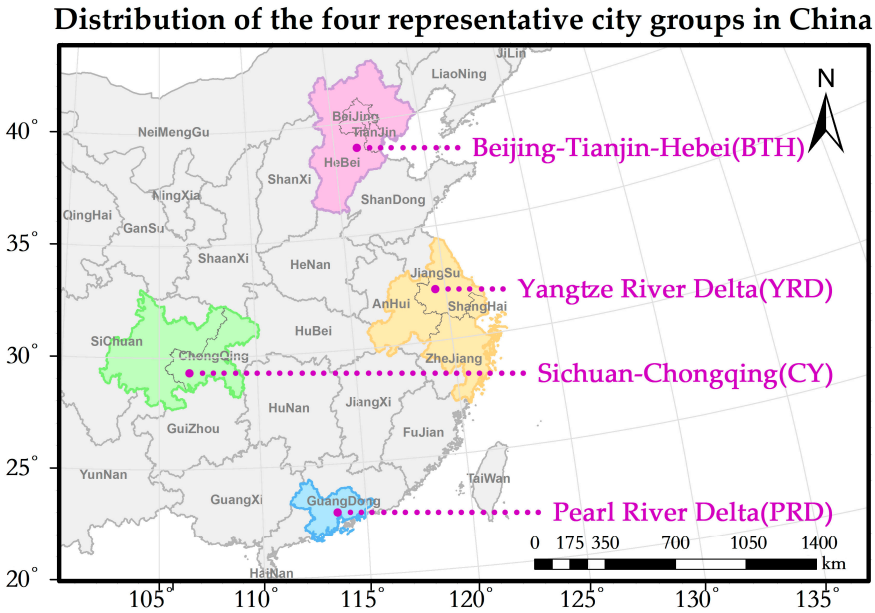


Figure 1. Distribution of the four representative city groups in China.

The BTH and YRD serve as major centers for heavy industry and manufacturing; the PRD, characterized by its warm and humid climate, is influenced by both biogenic and anthropogenic emissions; while the CY region, located in a basin with complex topography, facilitates the accumulation of pollutants under stagnant weather conditions. These differences make the four regions representative case studies for investigating ozone formation sensitivity in varying environmental contexts.

2.2. Ground-Based Observation

Since 2012, the China National Environmental Monitoring Centre (CNEMC), established by the Ministry of Ecology and Environment of China, has been responsible for national environmental quality monitoring. It encompasses domains such as the atmosphere, water bodies, soil, and noise, providing crucial support for environmental governance, policy-making, and scientific research through real-time, ground-based monitoring data. Currently, CNEMC has established 1734 urban air quality monitoring stations nationwide (Figure 2). These stations are distributed across various environmental settings, including urban roadsides, parks, and industrial areas, ensuring a diversified monitoring of pollutant concentrations, including ozone.

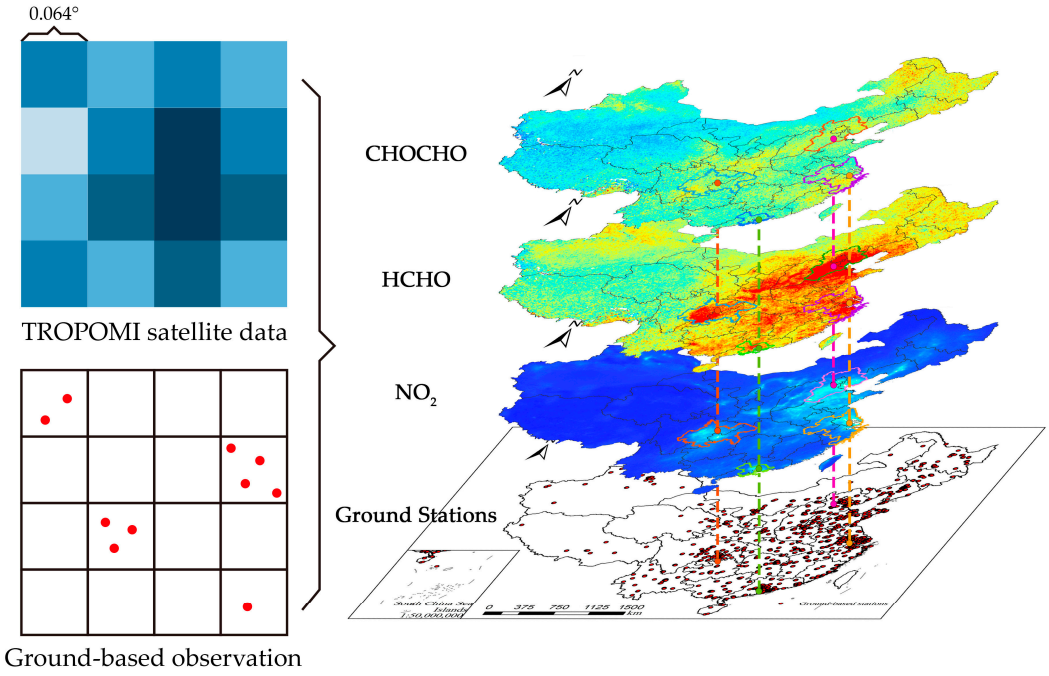


Figure 2. Map combining satellite data with monitoring data from ground stations.

The ground-based monitoring data used in this study consist of hourly ozone concentration data (O_3-1h) provided by CNEMC, sourced from four major urban agglomerations: the Beijing–Tianjin–Hebei (BTH, 69 sites), the Yangtze River Delta (YRD, 209 sites), the Pearl River Delta (PRD, 56 sites), and the Sichuan–Chongqing (CY, 95 sites). The data cover the period from 2020 to 2024. For this study, O_3-1h data from 13:00 and 14:00 local time daily were selected to calculate the average ozone concentration at each station, which was then matched with TROPOMI satellite data [30,31]. To ensure reliability, the data underwent quality control, including the removal of missing values and outliers.

This dataset is characterized by several key advantages. Its high temporal resolution (hourly) allows for the capture of peak afternoon ozone concentrations during periods of active photochemical reactions, which aligns well with TROPOMI's overpass time. The extensive spatial coverage, with stations in urban centers, suburbs, industrial areas, and rural settings, reflects ozone concentration disparities arising from different emission sources and meteorological conditions. The data quality is stable, with O_3 measurements having a precision of approximately ±5–10 ppb according to China's environmental protection standards. However, quality control is still necessary to filter out anomalies caused by local pollution events or meteorological interferences. When combined with TROPOMI's NO_2, HCHO, and CHOCHO column concentrations, these ground-based O_3 data are exceptionally well-suited for analyzing the ozone sensitivity classifications of FNR and GNR. This is particularly valuable for studying spatiotemporal variations in the complex atmospheric environments of urban agglomerations, thereby providing a scientific basis for the precise formulation of regional ozone control strategies.

2.3. TROPOMI Satellite Data

The VCD satellite data for NO_2, HCHO and CHOCHO used in this study are from the Sentinel-5P Level 2 data product, which can be downloaded free of charge from the European Space Agency's Sentinel Science Data Center (https://dataspace.copernicus.eu accessed on 9 May 2025).

Sentinel-5P launched by the European Space Agency in 2017, is a satellite dedicated to global atmospheric pollution monitoring [32]. Its atmospheric monitoring instrument,

TROPOMI (Tropospheric Monitoring Instrument), can effectively observe a variety of atmospheric trace gases on a global scale, including NO_2, HCHO, and CHOCHO [29,33]. The relative error of the tropospheric NO_2 vertical column density (VCD) is about 30–50% in polluted regions, with a precision of about 5.0–6.0 $\times$ 10^{14} molecules cm^{-2} [34]. The relative error of the HCHO VCD is about 20–40% in polluted regions, with a precision of about 0.5–1.5 $\times$ 10^{15} molecules cm^{-2} [35,36]. The relative error for the CHOCHO VCD is higher, at approximately 30–70%, with a precision of about 1.0–3.0 $\times$ 10^{14} molecules cm^{-2}, due to its low concentration and spectral interference [29]. These high-resolution data provide reliable support for the spatiotemporal distribution analysis of trace gases.

TROPOMI provides daily global coverage and is able to revisit the same geographic region once a day, thus significantly improving the temporal resolution of atmospheric observations, with a transit time of 13:30 per day in China, a spatial resolution of 0.064° $\times$ 0.064°, and a screened data quality of QA value $\geq$ 0.5. The TROPOMI data used in this study span from 1 January 2020 to 31 December 2024. Figure 2 shows the method of combining satellite data with ground station monitoring data.

2.4. Methods

The method for determining threshold ranges for FNR and GNR was adapted from the approach established by Jin et al. [12,37], with modifications to account for data characteristics and uncertainty propagation.

Data preprocessing and uncertainty considerations. A regular 0.064° $\times$ 0.064° grid was constructed to cover the study area. Daily TROPOMI retrievals of HCHO (precision: 0.5–1.5 $\times$ 10^{15} molecules cm^{-2}, relative error: 20–40%), CHOCHO (precision: 1.0–3.0 $\times$ 10^{14} molecules cm^{-2}, relative error: 30–70%), and NO_2 (precision: 5.0–6.0 $\times$ 10^{14} molecules cm^{-2}, relative error: 30–50%) were reprojected onto this grid [29,34–36]. Ground-based O_3 monitoring data were obtained from CNEMC stations with a measurement precision of $\pm$5–10 ppb according to national environmental monitoring standards.

Spatiotemporal matching and quality control. Ground-based monitoring stations were assigned to their corresponding grid cells based on geographic coordinates. Hourly O_3 measurements were averaged over the 13:00–14:00 local time window to match the satellite overpass time (13:30 local time). When multiple stations resided within one cell, their O_3 observations were averaged to ensure spatial consistency (Figure 2). To mitigate the influence of outliers, FNR and GNR values were truncated at the 1st and 99th percentiles, reducing the impact of extreme values on statistical analysis.

Statistical analysis and threshold determination. The collocated O_3-FNR and O_3-GNR pairs were grouped into 100 bins according to the satellite-derived ratios, and the average O_3 concentration was computed for each bin. A seventh-order polynomial regression was employed to capture the non-linear relationship between binned O_3 and the sensitivity indices, as lower-order polynomials failed to reproduce the peak structure of the O_3-GNR relationship (Figure S1). The ozone maximum was identified mathematically at the point where the first derivative of the fitted curve was zero and the second derivative was negative.

The transition regime was defined as the FNR or GNR interval encompassing the top 10% of O_3 values on the fitted curve [12,38]. The lower and upper bounds of this interval set the thresholds for classifying VOC-limited (below the lower bound) and NO_x-limited (above the upper bound) regimes [39].

3. Results

3.1. Ozone Pollution Characteristics

China's urban agglomerations exhibit distinct ozone pollution patterns due to their unique meteorological conditions and precursor emission characteristics. To delve deeper into the complex chemical responses between O_3 and its precursors in each region and analyze their current pollution status, this study plots the monthly distribution of O_3 concentrations for each urban agglomeration using boxplots based on ground-based observation data.

We compiled statistics on the distribution of ozone concentrations for each urban agglomeration across different months. Figure 3 shows the results of the monthly ozone concentration distribution in the study areas. It is evident that there are differences in ozone pollution among the various regions. The Beijing–Tianjin–Hebei (BTH) region, the Yangtze River Delta (YRD), and the Chengdu–Chongqing (CY) urban agglomeration primarily experience ozone pollution from May to September, which corresponds to the peak ozone pollution season in China. Furthermore, according to local climatological data, the Pearl River Delta (PRD) exhibits elevated ozone concentrations throughout the year with less distinct seasonal characteristics, and its O_3 pollution mainly occurs from August to October. Among these regions, the BTH region suffers from the most severe O_3 pollution due to the combined effects of human activities and natural conditions. The peak month for O_3 pollution in the BTH region is June, with the median ozone concentration in the boxplot exceeding 160 $\mu g/m^3$.

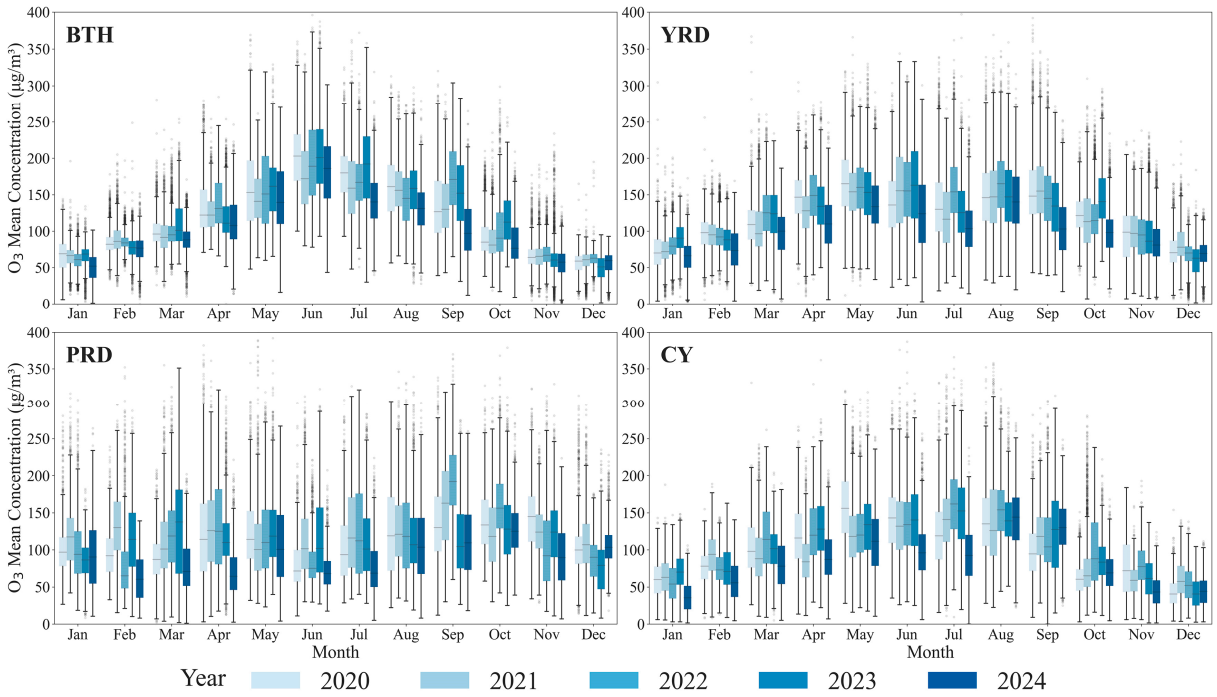


Figure 3. Boxplot distribution of monthly ozone concentrations in four typical urban agglomerations of China (BTH, YRD, PRD, and CY) from 2020 to 2024.

3.2. Spatiotemporal Variations in Ozone Precursors and Indicator Indices

Ground-level O_3, a major secondary pollutant, is formed through complex chemical reactions involving its precursors: NO_x and VOCs. The relationship between O_3 and its precursors is not a simple positive linear correlation but exhibits highly non-linear characteristics. Consequently, the ozone pollution status of a region is fundamentally determined by the spatiotemporal distribution patterns of its precursors.

This study utilizes TROPOMI satellite data to systematically analyze the spatiotemporal distribution and seasonal variations in key O_3 precursors—NO_2, as well as formaldehyde (HCHO) and glyoxal (CHOCHO) as proxies for VOCs—across four major urban agglomerations in China: the Beijing–Tianjin–Hebei region (BTH), the Yangtze River Delta (YRD), the Pearl River Delta (PRD), and the Chengdu–Chongqing urban agglomeration (CY). Figure 4 visually presents the monthly average column concentrations of these precursors.

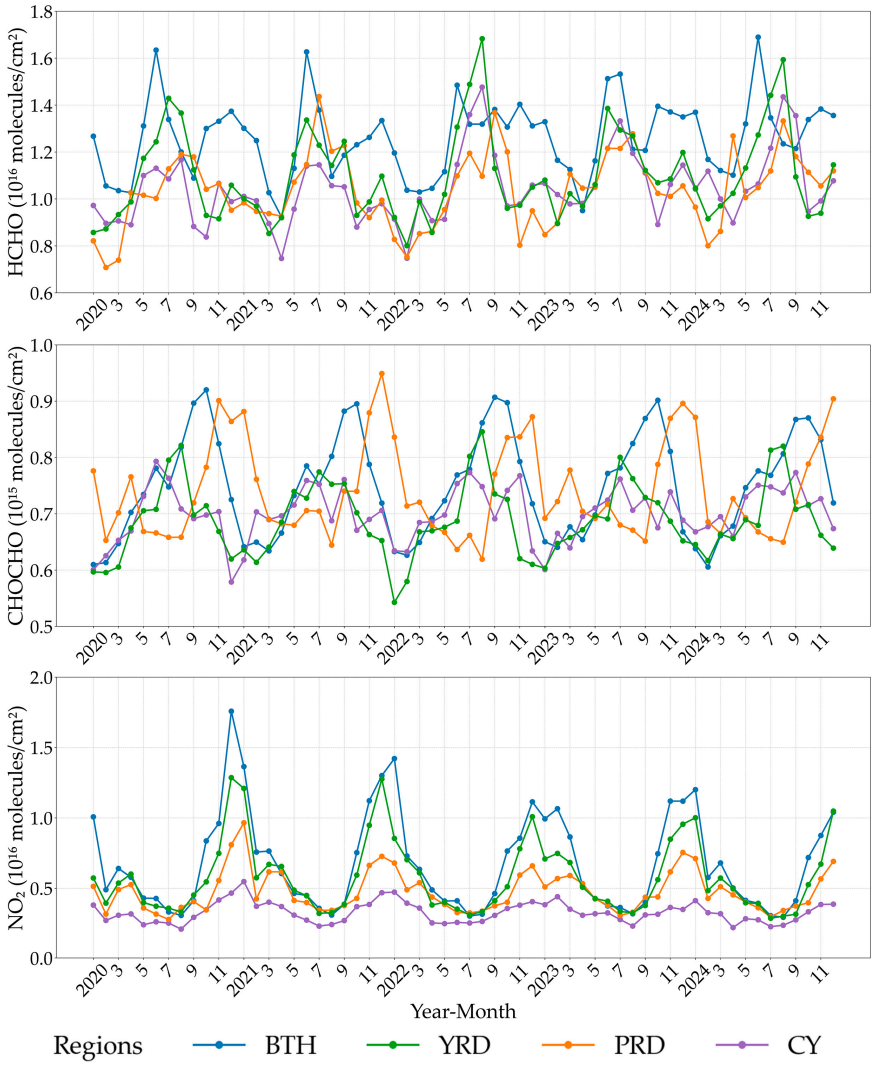


Figure 4. Temporal variation in tropospheric HCHO, CHOCHO and NO_2 column concentrations from January 2020 to December 2024 in BTH, YRD, PRD and CY.

HCHO has two peaks in its annual variation: one in early summer (June–July), representing the highest levels of the year, and another smaller peak in November. In contrast, HCHO concentrations are lowest during the winter months. The maximum HCHO concentrations for each region were 1.69×10^{16} molecules/cm^2 in BTH (June 2024), 1.68×10^{16} in YRD (August 2022), 1.43×10^{16} in PRD (July 2021), and 1.48×10^{16} in CY (August 2022). The corresponding minimum values were 9.23×10^{15} in BTH (April 2021), 8.01×10^{15} in YRD (February 2022), 7.08×10^{15} in PRD (February 2020), and 7.47×10^{15} in CY (April 2021).

CHOCHO shows a distinct seasonal cycle, though its peak and trough timings vary across the four regions. The highest monthly average concentrations were observed in PRD (9.49×10^{14} molecules/cm^2, December 2021), followed by BTH (9.20×10^{14}, October 2020),

YRD (8.46×10^{14}, August 2022), and CY (7.93×10^{14}, June 2020). The lowest values were 6.06×10^{14} in BTH (February 2024), 5.43×10^{14} in YRD (January 2022), 6.19×10^{14} in PRD (August 2022), and 5.79×10^{14} in CY (December 2020).

NO_2 concentrations show a typical seasonal pattern with higher values in winter and lower values in summer, primarily driven by seasonal changes in photochemical activity, emission intensity, and meteorological conditions. The maximum NO_2 concentrations were recorded as 1.76×10^{16} molecules/cm^2 in BTH (December 2020), 1.29×10^{16} in YRD (December 2020), 9.65×10^{15} in PRD (January 2021), and 5.47×10^{15} in CY (January 2021). The lowest values were 2.94×10^{15} in BTH (August 2024), 2.87×10^{15} in YRD (July 2024), 2.79×10^{15} in PRD (July 2020), and 2.10×10^{15} in CY (August 2020).

Figure 5 illustrates the temporal variations in FNR ($HCHO/NO_2$) and GNR ($CHOCHO/NO_2$) exhibit distinct seasonal patterns, with higher values in summer and lower values in winter. Notably, the CY region consistently shows higher FNR and GNR values compared to other regions. The maximum FNR values across the regions are: 4.48 in BTH (July 2024), 5.27 in YRD (August 2024), 4.49 in PRD (July 2021), and 6.12 in CY (August 2024). The minimum FNR values are: 1.04 in BTH (December 2020), 0.86 in YRD (December 2020), 1.16 in PRD (January 2021), and 1.93 in CY (February 2022). For GNR, the maximum values are: 0.29 in BTH (August 2024), 0.29 in YRD (July 2024), 0.25 in PRD (July 2020), and 0.36 in CY (July 2024). The minimum GNR values are: 0.06 in BTH (December 2024), 0.05 in YRD (December 2024), 0.10 in PRD (January 2021), and 0.12 in CY (January 2021).

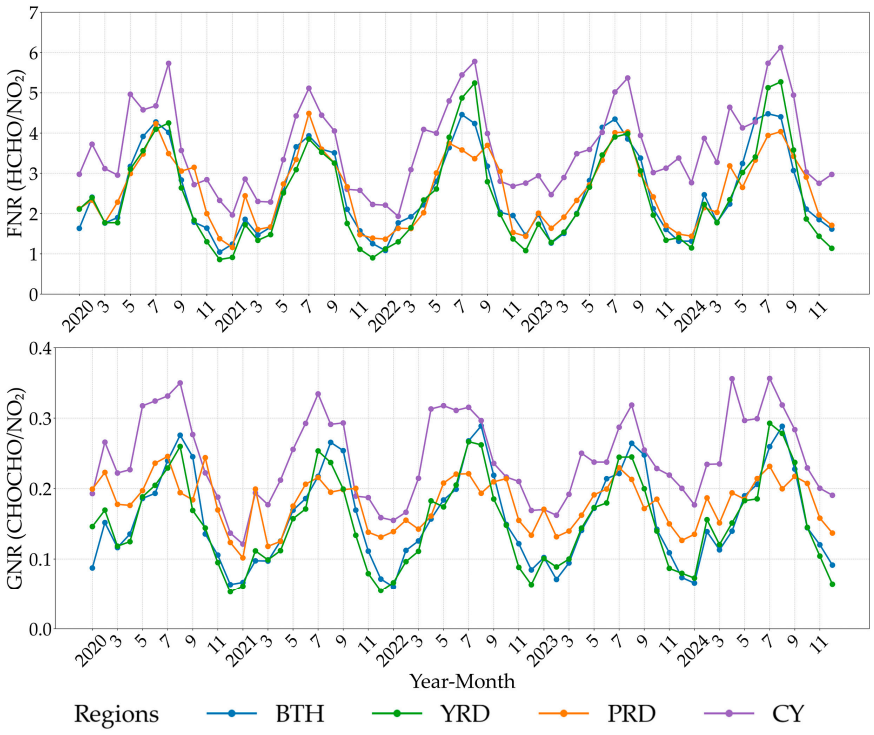


Figure 5. Temporal variation in the ozone sensitivity indices FNR and GNR in the BTH, YRD, PRD, and CY regions from January 2020 to December 2024.

Figure 6 further illustrates the spatial distribution of average HCHO, CHOCHO and NO_2 concentrations during the summer (June–August) and autumn (September–November) of 2023. Spatially, HCHO and NO_2 are primarily concentrated in the central areas of major urban agglomerations, showing clear urban-centered distribution patterns. In contrast, CHOCHO exhibits a more uniform spatial distribution across regions, with less apparent clustering in urban cores. Seasonally, HCHO concentrations are higher in summer than in autumn, while CHOCHO shows slightly higher average concentrations

in autumn. NO_2 concentrations are consistently higher in autumn than in summer across all regions.

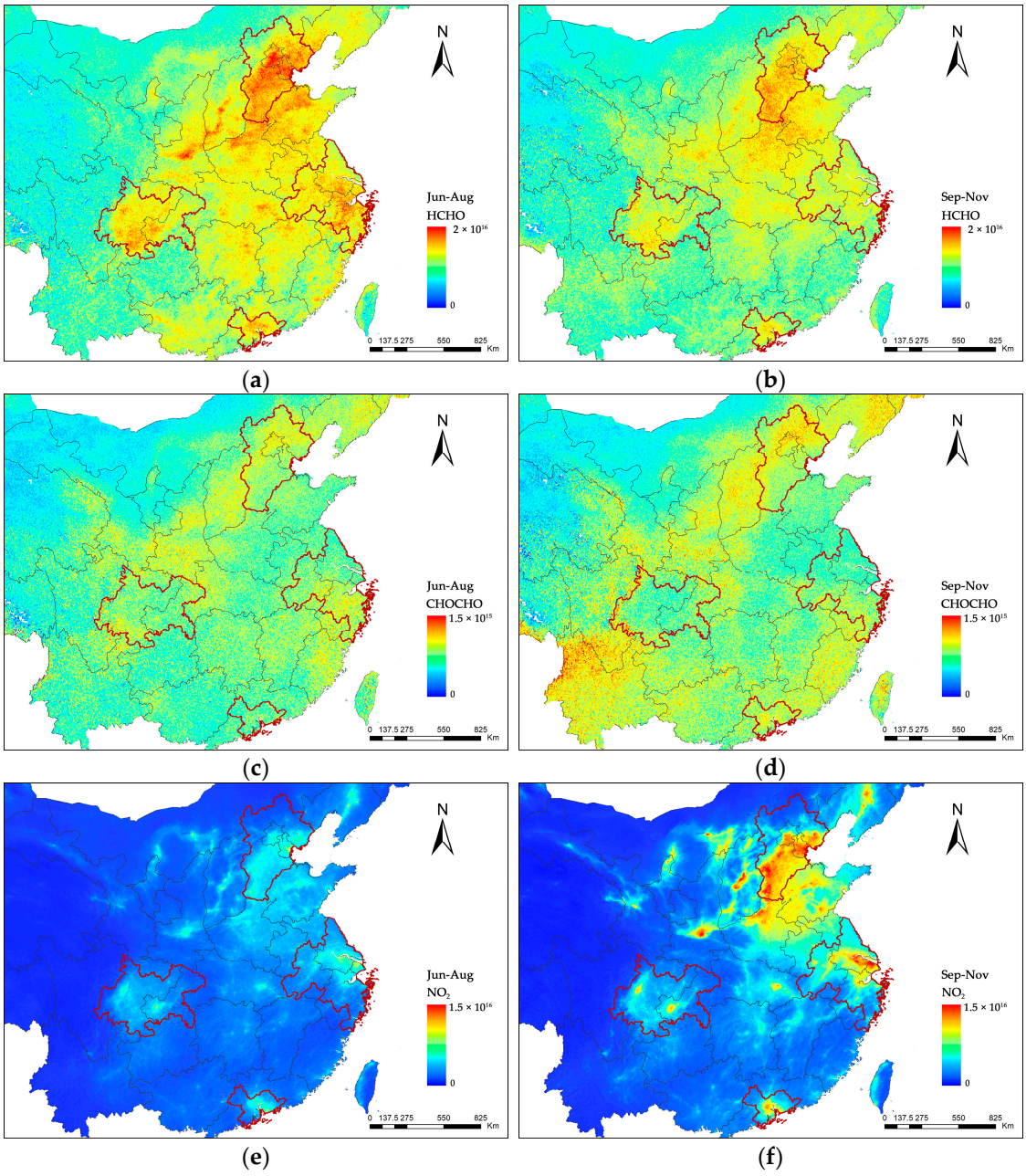


Figure 6. Spatial distribution of ozone precursors in summer and autumn 2023: (**a**,**b**) HCHO; (**c**,**d**) CHOCHO; and (**e**,**f**) NO_2.

3.3. Threshold Determination of FNR and GNR

The relationship between O_3 and its precursors is highly non-linear, creating distinct chemical regimes [40]. To diagnose these regimes from space, the ratio of formaldehyde to nitrogen dioxide (FNR) has been established as a robust indicator. A region is classified as VOC-limited when its FNR value is below a defined lower threshold, indicating that O_3 production is more sensitive to changes in VOCs. Conversely, a region is classified as NO_x-limited when its FNR value exceeds an upper threshold, where O_3 concentrations are more sensitive to NO_x levels [41,42]. Regions with FNR values between these thresholds are considered transitional, where O_3 concentrations are transition regime led by both NO_x and VOCs [43]. Figure 7 illustrates the relationship between FNR, GNR, and ground-level

O_3 concentrations in China during the summer and autumn of 2023. We analyzed the relationships between FNR, GNR, and O_3 to identify control regimes.

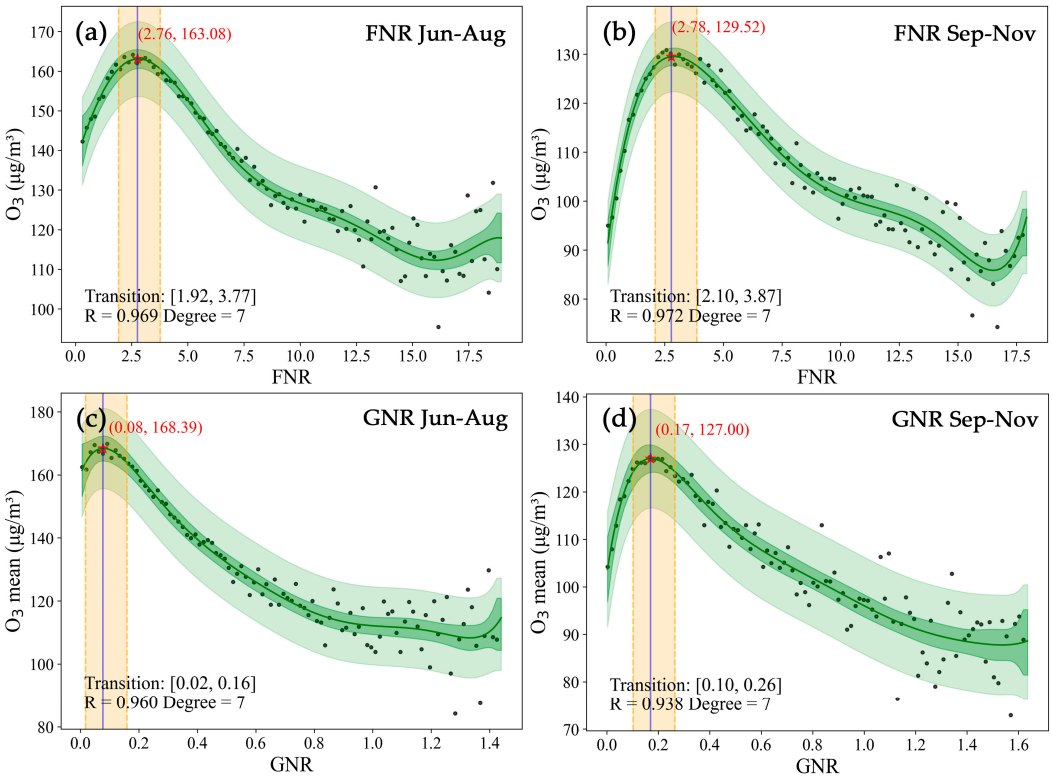


Figure 7. (**a**,**b**) show the classification of control regimes based on the ozone sensitivity index FNR in summer and autumn 2023, while (**c**,**d**) show the same for GNR. The green solid line is the fitted seventh-order polynomial curve and the shadings represent 95% confidence and 95% prediction bands, respectively. The blue solid line represents the peak of the fitted curve, the red star represents the highest point of the fitted curve, and the orange vertical shading indicates the range over the top 10% of the fitted curve (transition regime).

Since ozone pollution in China typically occurs in summer and autumn, we selected data from these seasons in 2023 to determine FNR and GNR thresholds. To ensure accuracy, we used the quantile method to remove extreme outliers, preventing their influence on the fitted curves. Figure 7 presents the results of determining FNR and GNR thresholds for the 2023 ozone pollution season, using high-order polynomial fitting with an R-value greater than 0.93. The top 10% of the fitted curves were designated as the transitional control zone. Across seasons, FNR and GNR thresholds increase from summer to autumn. The FNR threshold rises from 1.92–3.77 in summer to 2.10–3.87 in autumn, while the GNR threshold increases from 0.02–0.16 in summer to 0.10–0.26 in autumn.

3.4. Spatial Classification of Ozone Formation Sensitivity

In summer both FNR and GNR are dominated by NO_x-limited and transition regimes. The transition regime in FNR is larger than that in GNR, and the VOC-limited regimes are almost absent (Figure 8a,b). In the middle of summer to fall, most of the transition regimes changed to VOC-limited, and the area around the city cluster changed from NO_x-limited areas to transition regimes, and the spatial distributions of the control types of FNR and GNR were similar, with VOC-limited in the center of the city, transition regimes around the city, and NO_x-limited areas in the other areas (Figure 8c,d). The relationship between FNR thresholds and their best-match GNR thresholds (Figure 8e).

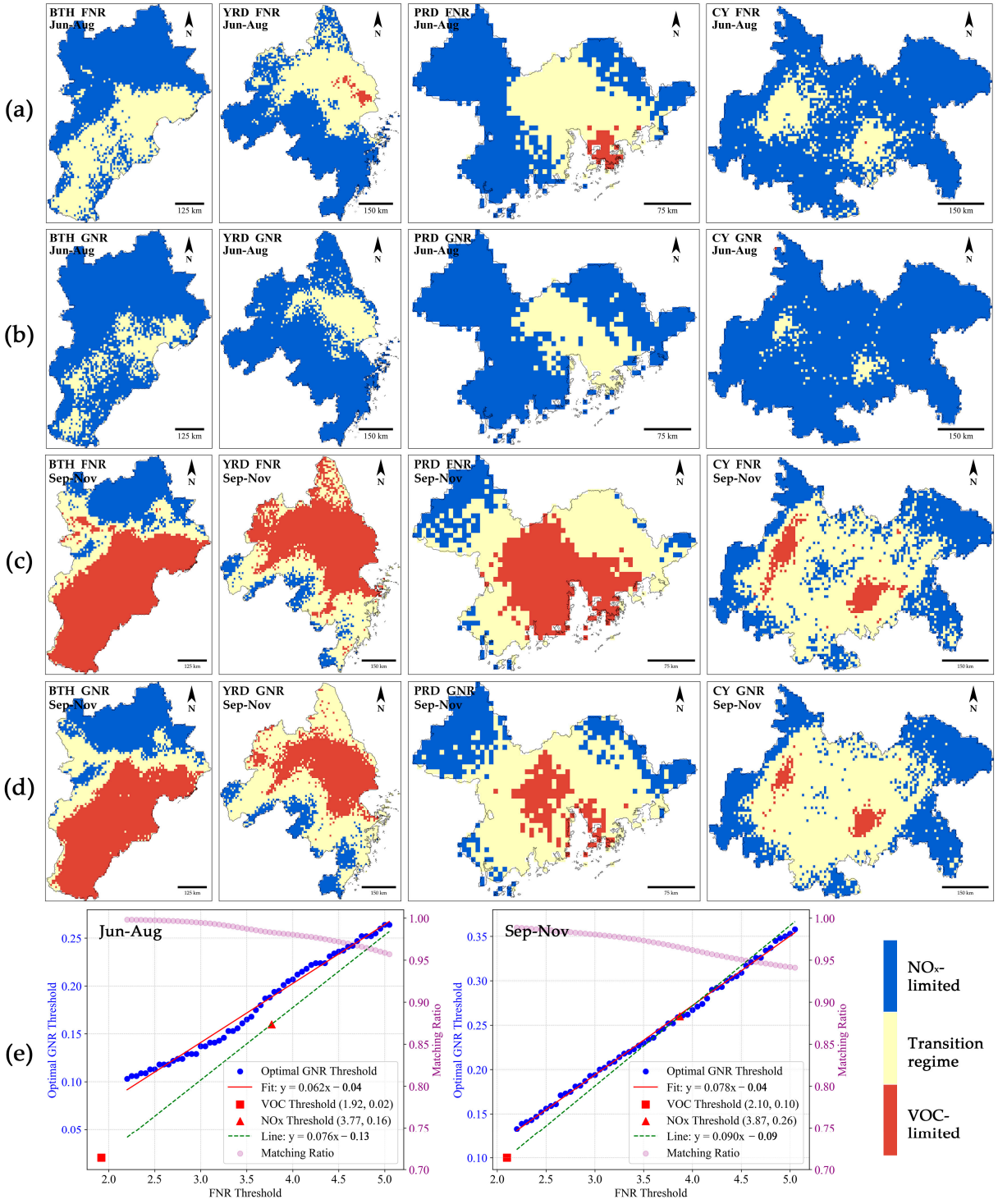


Figure 8. Spatial distribution maps of ozone sensitivity indices FNR, GNR and precursors during the ozone pollution severity seasons. Spatial distribution of (**a**) FNR [1.92, 3.77], (**b**) GNR [0.02, 0.16], (**c**) FNR [2.10, 3.87], (**d**) GNR [0.10, 0.26] in ozone sensitive control area types in summer and autumn. (**e**) The relationship between FNR thresholds and their best-match GNR thresholds. The blue points represent optimal GNR thresholds for FNR thresholds, accompanied by a red fitted line. Red markers indicate VOC-limited and NO_x-limited thresholds, which are connected by a green dashed line. The purple scatter illustrates the matching ratio between FNR and GNR classifications.

To investigate the differences in threshold-based classification between FNR and GNR, we identified the GNR threshold that maximizes the matching ratio for each FNR threshold. For a given FNR threshold, the spatial distribution of FNR is classified into three categories:

above, equal to, and below the threshold, and the GNR threshold yielding the most similar classification is determined. As shown in Figure 8e, a linear relationship exists between FNR and GNR thresholds. The VOC threshold (distinguishing VOC-limited from transition regime) shows a larger discrepancy between FNR and GNR classifications compared to the NO_x threshold (distinguishing NO_x-limited from transition regime).

Specifically, the GNR VOC threshold, determined using the top 10% fitted curve method, is lower than the FNR threshold with the highest classification similarity, while the NO_x threshold exhibits higher similarity between FNR and GNR classifications. The matching ratio decreases as the FNR threshold increases, dropping from approximately 99% to 95%.

3.5. Comparison of FNR and GNR Ozone Formation Sensitivity

Figure 9 illustrates the spatial distribution of ozone sensitivity classifications, comparing results from FNR and GNR across China's four major urban agglomerations during summer and autumn of 2023. Significant regional and seasonal differences between the two indicators are evident. This difference also exists in other years, as shown in Figures S7 and S8.

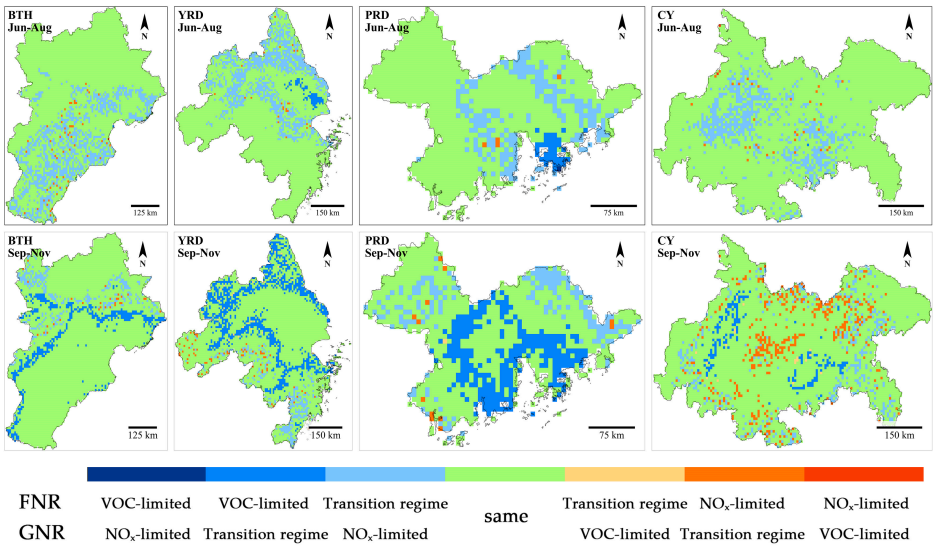


Figure 9. Differences in ozone precursor control regimes between FNR and GNR across four major urban agglomerations in China in 2023.

During the summer months, the control types in the urban cores of BTH and CY are consistently classified as transition regime by both indicators. In contrast, the urban centers of YRD and PRD show a divergence, where FNR indicates VOC-limited conditions while GNR identifies them as transition regime. A notable feature across all agglomerations is the prevalence of light-blue areas in the peripheries. In these regions, FNR designates a transition regime, while GNR classifies them as NO_x-limited regions, indicating that GNR has a stronger tendency toward such areas.

In the autumn, the central and surrounding areas of BTH, YRD, and PRD generally show consistent classifications between the two indicators. However, significant differences emerge in regions near the classification thresholds. In these transitional regime areas, areas identified by FNR as VOC-limited are classified as transition regime by GNR, and those identified as transition regime by FNR are classified as NO_x-limited by GNR. This pattern further substantiates that GNR is more biased towards an NO_x-limited designation than FNR. In the suburban areas of CY, a different type of discrepancy is observed, with many regions being classified as NO_x-limited by FNR but as transition regime by GNR. We found

similar differences between the two indicators in other years of our study. This indicates that these discrepancies reflect the characteristics of FNR and GNR in their response to different emission sources.

By counting the percentage of ozone precursor control types in different indices of the four major urban agglomerations in China in summer and fall. As shown in Table 1, it can be seen that in the summer the urban agglomerations are dominated by NO_x-limited and transition region, with the GNR preferred to NO_x-limited. In the fall these areas are dominated by VOC-limited or transition region, with the GNR preferred to classify them as NO_x-limited and transition region.

Table 1. Statistics on the percentage of ozone precursor control types in the four major urban agglomerations in China with different indices in the summer and fall seasons.

City	O_3 Formation Region	June to August		September to November	
		FNR (%)	GNR (%)	FNR (%)	GNR (%)
BTH	VOC	0.02	0	55.09	47.09
	VOC-NO_x	40.18	20.51	20.18	23
	NO_x	59.80	79.49	24.73	29.91
YRD	VOC	1.54	0	52.34	32.95
	VOC-NO_x	39.24	19.22	38.22	53.34
	NO_x	59.21	80.78	9.44	13.71
PRD	VOC	3.09	0	35.67	13.03
	VOC-NO_x	38.18	23.39	48.04	57.31
	NO_x	58.73	76.61	16.29	29.66
CY	VOC	0.02	0.04	6.45	3.39
	VOC-NO_x	18.29	4.37	54.17	56.85
	NO_x	81.29	95.59	39.38	39.76

This Figures S3–S6 illustrate the spatial distributions of FNR and GNR across the BTH, YRD, PRD, and CY city clusters during summer and autumn. Using a 3×3 moving window, the local minimum of each index is identified and treated as the center, around which the relationship between index values and distance from the center is analyzed. Results show that the centers generally align with urban cores—for instance, Tianjin in BTH, Shanghai in YRD, Hong Kong in PRD, and Chongqing in CY. The spatial extent of influence varies with city scale, BTH is set at 200 km, YRD at 250 km, and PRD and CY at 150 km.

As the values of FNR and GNR increase, the distance from the center also increases, exhibiting similar trends for both indices. Notably, the gradient between the center and periphery is smaller in summer than in autumn, indicating a more gradual transition of control regimes during the summer season.

Figure 10 presents the threshold-based differences between FNR and GNR as a function of distance from the center. It is evident that GNR thresholds are typically reached closer to the center than FNR thresholds, resulting in a spatial offset between the two. This implies that GNR tends to classify more areas as NO_x-limited compared to FNR.

To further evaluate the reliability of FNR and GNR across different environments, we compared our classification results with those from existing field observations and modeling studies (Table 2).

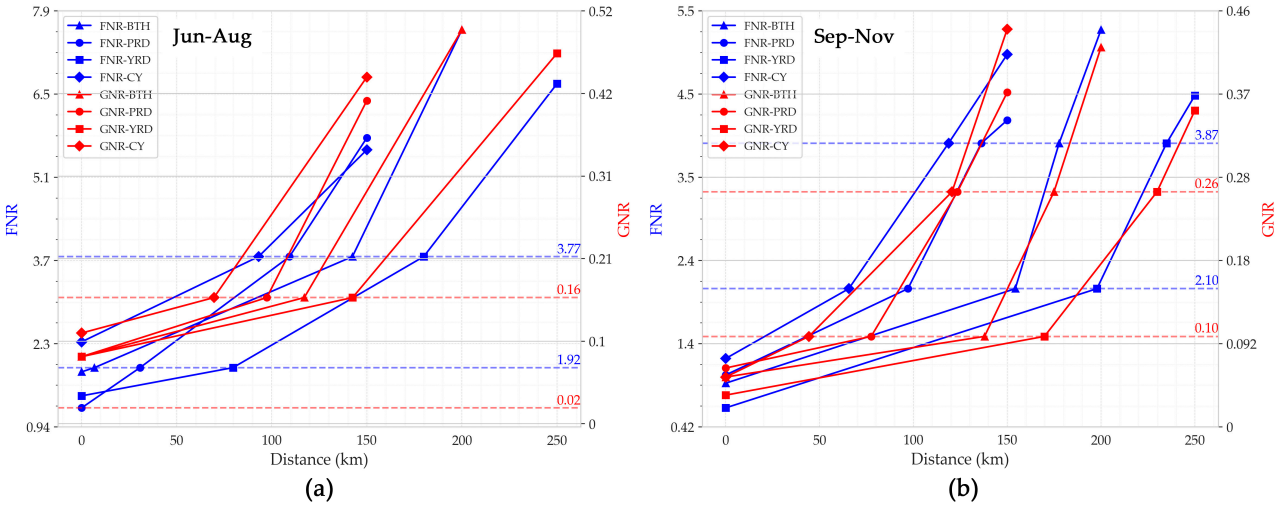


Figure 10. Relationship between thresholds and distances from city centers for BTH, YRD, PRD, and CY in (**a**) summer and (**b**) autumn of 2023.

Table 2. Comparison of OFS studies in the regions of China.

No.	Observation Period	Site Location	Site Type	Method	FNR	GNR	Ozone Formation Region	Reference
1	17–23 August 2020	Nanjing (YRD)	Urban	CMAQ&OBM	Transition region	Transition region	Transition region	Li et al., 2022 [44]
2	24 August to 11 October 2018	Changzhou (YRD)	Urban	EKMA	VOC-limited	VOC-limited	VOC-limited	Liu et al., 2023 [45]
3	September to November 2018	Guangzhou (PRD)	Urban	Chemical box model & EKMA	VOC-limited	VOC-limited	VOC-limited	Zhao et al., 2022 [46]
4	July 2019	Zhengzhou	Urban	OBM	Transition region	Transition region	VOC-limited & Transition region	Wang et al., 2023 [47]
5	26–30 September 2021	Guangzhou (PRD)	Urban	CMAQ	VOC-limited	VOC-limited	VOC-limited	Wang et al., 2023 [48]
6	29 August to 3 September 2020	Huadu (PRD)	Suburban	EKMA	VOC-limited	Transition region	VOC-limited	Wang et al., 2023 [49]
7	2014–2019	Hongkong	Urban& Suburban	RIR& EKMA	VOC-limited	VOC-limited	VOC-limited	Zeng et al., 2022 [50]
8	August 2022	Chengdu & Chongqing (CY)	Urban	OBM	Transition region	Transition region	VOC-limited& Transition region	Wang et al., 2024 [51]
9	June to August 2019	Chengdu (CY)	Urban	EKMA	VOC-limited	VOC-limited	VOC-limited	Wang et al., 2023 [52]
10	June to August 2020	Shijiazhuang (BTH)	Urban	PMF	Transition region	Transition region	VOC-limited	Guan et al., 2023 [53]
11	September 2020 to February 2021	Shenzhen (PRD)	Suburban	VOCs/NO_x ratio	Transition region	NO_x-limited	NO_x-limited	Zhang et al., 2023 [54]
12	10 August to 10 September 2019	Chengdu (CY)	Suburban	RIR	Transition region	Transition region	VOC-limited	Li et al., 2023 [55]

In many urban areas, FNR and GNR both showed strong agreement with previously reported sensitivity classifications. For instance, studies in Guangzhou conducted by Zhao et al. [46] using chemical box models and by Wang et al. [48] using the CMAQ model consistently diagnosed VOC-limited conditions, which were fully confirmed by both FNR and GNR in our results. Similar consistency was observed in Changzhou, as reported by Liu et al. [45], and in Hong Kong, as noted by Zeng et al. [50], where the regime was also identified as VOC-limited by both satellite indicators and the literature. In Nanjing, Li et al. [44] reported a transitional regime based on CMAQ and OBM modeling, which was correctly captured by both FNR and GNR, indicating their reliability under transitional chemical environments.

There were instances where FNR and GNR produced the same classification, yet this classification did not align with the conclusions of previous studies. For instance, in Shijiazhuang, Guan et al. [53] identified a VOC-limited regime using PMF, while both FNR

and GNR indicated a transitional regime. A similar discrepancy occurred in suburban Chengdu, where Li et al. [55] reported VOC-limited sensitivity, but both indicators again suggested a transitional regime. These inconsistencies may be attributed to spatial scale mismatches or the inability of satellite indicators to capture fine-scale VOC enrichment in areas with complex terrain or meteorological conditions.

In some suburban and urban-fringe areas, FNR and GNR produced different results, with only one of them aligning with literature-based classifications. In Huadu (PRD), Wang et al. [49] diagnosed a VOC-limited regime using EKMA, which was confirmed by FNR, whereas GNR suggested a transition regime, possibly due to its stronger sensitivity to NO_2 variability. In contrast, in Shenzhen, Zhang et al. [54] identified a NO_x-limited regime based on the VOCs/NO_x ratio. GNR successfully captured this condition, while FNR misclassified it as a transition regime.

4. Discussion

A comparative analysis of different ozone sensitivity indices in representative regions of China is essential for identifying the primary drivers of ozone pollution and implementing corresponding control measures. This study systematically compares the ozone precursor control regimes defined by two satellite-based sensitivity indices, FNR and GNR, across four major urban agglomerations in China (BTH, YRD, PRD, and CY, Figure 1) during summer and autumn. The analysis reveals differences in the temporal and spatial distributions of the two indices.

In summer, the FNR classification indicates that urban areas are predominantly under transition regime, with some urban centers classified as VOC-limited. In contrast, the GNR classification identifies urban centers as transition regime, while most remaining areas are designated as NO_x-limited. The FNR index is based on the HCHO/NO_2 ratio. HCHO has both secondary sources from biogenic precursors (e.g., isoprene oxidation) and significant primary sources from anthropogenic activities (e.g., industrial emissions and vehicle exhaust) [56,57]. Although biogenic emissions increase during summer due to high temperatures and strong solar radiation, HCHO concentrations in urban areas are often higher than in suburban areas, indicating that anthropogenic emissions are the dominant factor driving urban HCHO levels [58]. Consequently, FNR is influenced by both HCHO and NO_2 in urban areas, leading to classifications of transition regime or VOC-limited regimes. The GNR index, which uses the CHOCHO/NO_2 ratio, is more sensitive to urban anthropogenic emissions because CHOCHO is primarily formed from the secondary oxidation of anthropogenic VOCs (e.g., aromatics, alkanes) [59]. In urban centers with high NO_2 concentrations, GNR values are low, resulting in classifications of VOC-limited or transition regime. In suburban areas with lower NO_2 levels, however, higher GNR values tend to classify these regions as NO_x-limited [24]. In autumn, the FNR classification identifies urban areas as VOC-limited, suburban areas as transition regime, and regions far from cities as NO_x-limited. The overall trend of the GNR classification is similar to that of FNR, but discrepancies exist in suburban areas: some regions classified as VOC-limited by FNR are designated as transition regime by GNR, and some areas classified as transition regime by FNR are identified as NO_x-limited by GNR [60]. This difference primarily arises from the distinct response mechanisms of GNR and FNR to changes in precursors [61]. While HCHO and CHOCHO concentrations are generally high in summer, both tend to decrease entering autumn. However, CHOCHO exhibits a counter-trend in some regions (such as BTH and PRD), with autumn levels slightly higher than in summer. The spatial distribution of the RGF (CHOCHO/HCHO) ratio in Figure S9 shows that this ratio is generally higher in autumn than in summer, indicating that although both HCHO and CHOCHO decrease from summer to autumn, the decline in CHOCHO is less

pronounced than that of HCHO. Therefore, in autumn, GNR is more likely than FNR to classify certain areas as NO_x-limited, exhibiting a stronger NO_x sensitivity. This tendency is more pronounced near the classification thresholds.

Furthermore, the interpretation of these satellite-derived indices must account for atmospheric vertical structure. The tropospheric column-average value may not accurately represent the chemical regime within the planetary boundary layer (PBL), where surface-level ozone production occurs. As demonstrated by chemical transport models such as Jin et al. [20] and Singh et al. [62], the PBL-FNR is often significantly lower (more VOC-limited) than the full-column FNR over urban areas. This vertical gradient arises because NO_2 concentrations are highly concentrated near the surface due to direct emissions, whereas HCHO, as a secondary pollutant, can be produced through VOC oxidation at various altitudes, leading to a more homogeneous vertical distribution. Consequently, the column FNR is effectively diluted by HCHO in the free troposphere, biasing it toward higher values (more NO_x-limited) than the actual near-surface regime. This vertical smoothing effect likely explains why strong NO_x emission sources in urban cores are frequently classified as "transitional" rather than unequivocally "VOC-limited" by column FNR. In contrast, the GNR may be less affected by this bias due to the tighter coupling between its anthropogenic VOC precursors and NO_x emissions within the PBL, making it a potentially more reliable indicator of near-surface chemistry in urban areas.

In summary, both FNR and GNR effectively reflect the spatiotemporal distribution of ozone control regimes in China's representative urban agglomerations [63]. They delineate a consistent spatial pattern that transitions from VOC-limited or transition regime conditions in urban cores to NO_x-limited conditions in suburban and rural areas. However, the two indicators exhibit certain differences rooted in their distinct chemical foundations. This discrepancy primarily arises from the different response mechanisms of their respective VOC proxies to various emission sources. FNR, which relies on HCHO, is responsive to both biogenic and anthropogenic emissions. This leads to a tendency during summer, a season of high temperatures and vigorous biogenic activity, to classify regions as either transition regime or VOC-limited. In contrast, GNR relies on CHOCHO, which is less influenced by biogenic sources and is more sensitive to urban anthropogenic emissions. As a result, it more readily classifies suburban areas as NO_x-limited, as shown in Figure 11.

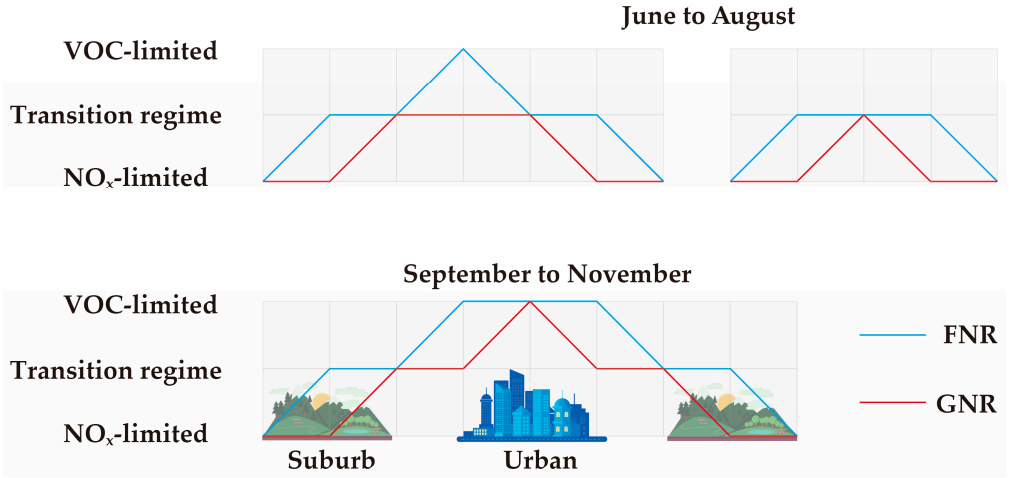


Figure 11. Characteristic map of the spatial distribution of ozone control types in summer and fall.

5. Conclusions

In this study, we utilized TROPOMI satellite-monitored tropospheric column densities of HCHO, CHOCHO, and NO_2 from 2020 to 2024, alongside ground-based observation data, to analyze the spatiotemporal characteristics of Ozone Formation Sensitivity (OFS) in

China's four major urban agglomerations: BTH, PRD, YRD, and CY. We also conducted a comparative analysis of two ozone sensitivity indices: FNR ($HCHO/NO_2$) and GNR ($CHOCHO/NO_2$).

The results indicate that tropospheric concentrations of CHOCHO, HCHO, and NO_2 exhibit distinct periodic variations. Higher column densities of HCHO and CHOCHO were consistently observed in summer, whereas higher NO_2 concentrations predominated in winter, leading to pronounced cyclical changes in the FNR and GNR indices. By correlating ground-level O_3 measurements with TROPOMI-derived FNR and GNR data, we assessed the regional and seasonal differences between these two indices. The variations in FNR and GNR reveal complex interactions among O_3 pollution sources, underscoring the importance of comparing different ozone sensitivity indicators. We determined the FNR and GNR thresholds for summer and autumn of 2023: FNR thresholds ranged from 1.92 to 3.77 in summer and 2.10 to 3.87 in autumn; GNR thresholds ranged from 0.02 to 0.16 in summer and 0.10 to 0.26 in autumn.

Furthermore, we analyzed the spatiotemporal characteristics of ozone control regimes as classified by FNR and GNR. While the two indices showed consistency in their spatial trends for OFS identification (Figures S3–S6), they differed in their threshold-based classifications and seasonal variations. A linear relationship exists between FNR and GNR thresholds, with greater classification discrepancies for the VOC threshold than for the NO_x threshold (Figure S2). Spatially, the minimum values for FNR and GNR typically appeared in urban centers, increasing with distance from the city core (Figures S3–S6). Seasonally, the differences were significant (Figure 10): in summer, urban centers were predominantly in a transitional state (with some VOC-limited areas in the urban centers of YRD and PRD), and the area classified as transitional by GNR was smaller than that identified by FNR. In autumn, both FNR and GNR shifted towards a VOC-limited regime in urban areas. Near the VOC threshold, GNR approached the transition regime, while near the NO_x threshold, the classifications for FNR and GNR were similar.

Regarding the relationship between thresholds and distance from the urban center (Figure 11), BTH, YRD, PRD, and CY exhibited similar patterns: in summer, GNR's NO_x threshold was at a shorter distance from the urban center than FNR's; in autumn, GNR's VOC threshold was at a shorter distance, while its NO_x threshold distance was similar to FNR's. Additionally, upon comparing our FNR and GNR classifications with other methods, we found that the results were identical in most cases, with discrepancies appearing in a few suburban areas, suggesting that GNR has a similar ozone formation sensitivity to FNR.

In conclusion, we have analyzed the spatiotemporal characteristics of OFS in China's four major urban agglomerations and compared the differences between the FNR and GNR ozone sensitivity indices. Our findings provide a valuable reference for ozone pollution control initiatives and deepen our understanding of different ozone sensitivity indicators. Future research should focus on integrating the advantages of both indicators to develop a more comprehensive method for identifying ozone sensitivity, thereby providing a theoretical basis for effective ozone control strategies.

Supplementary Materials: The following supporting information can be downloaded at https://www.mdpi.com/article/10.3390/rs17193321/s1; Figure S1: Changes in threshold ranges of FNR and GNR during the summer and autumn of 2023 and 2024 under different fitting orders; Figure S2: Scatter plot of FNR versus Optimal GNR Threshold and Matching Ratio for TROPOMI data from 2022-2024. The blue points represent optimal GNR thresholds for FNR thresholds, accompanied by a red fitted line. Red markers indicate VOC-limited and NOx-limited thresholds, which are connected by a green dashed line. The purple scatter illustrates the matching ratio between FNR and GNR classifications; Figure S3: Spatial distribution of FNR and GNR in BTH and the relationship between FNR GNR and the distance to the lowest point. (a)(b)(c)(d) June to August (e)(f)(g)(h) September to

November; Figure S4: Same as Figure S3, but for YRD; Figure S5: Same as Figure S3, but for PRD; Figure S6: Same as Figure S3, but for CY; Figure S7: Differences in ozone precursor control regimes between FNR and GNR across four major urban agglomerations in China in 2022; Figure S8: Same as Figure S7, but for 2024; Figure S9: Spatial distribution of RGF (CHOCHO/HCHO) in four major Chinese cities in 2023 (a) June to August (b) September to November.

Author Contributions: Conceptualization, L.C., J.T. and M.F.; formal analysis, J.F.; methodology, J.F., Y.L. and C.Y.; writing—original draft preparation, J.F.; writing—review and editing, C.Y., Y.Z. and J.F. All authors have read and agreed to the published version of the manuscript.

Funding: This research was funded by the National Key Research and Development Program of China (Grant No. 2023YFC3705801), National Natural Science Foundation of China (Grant No. 42171393), and Services of Guangdong Ecological and Environmental Monitoring Centre (ZXCG-2024-161).

Data Availability Statement: The Sentinel-5P TROPOMI satellite data used in this study, including HCHO, CHOCHO, and NO_2 Level-2 products, are publicly available. HCHO and NO_2 can be downloaded from https://disc.gsfc.nasa.gov/ (accessed on 9 May 2025), and CHOCHO can be accessed at https://data-portal.s5p-pal.com/ (accessed on 9 May 2025). Near-surface ozone observation data were obtained from the China National Environmental Monitoring Center, which can be downloaded at http://www.cnemc.cn/ (accessed on 9 May 2025). This center provides daily air quality data for major cities across China. All processed data supporting the findings of this study are available from the corresponding author upon reasonable request.

Acknowledgments: We would like to thank the following agencies for providing the satellite data: The TROPOMI Level 2 NO_2 product and TROPOMI Level 2 HCHO product were developed by the Royal Netherlands Meteorological Institute (KNMI), while the TROPOMI Level 2 CHOCHO (glyoxal) product was developed by the Royal Belgian Institute for Space Aeronomy (BIRA-IASB) with collaborative support from KNMI. These products were developed with funding from the Netherlands Space Office (NSO), processed with funding from the European Space Agency (ESA). We also thank the China National Environmental Monitoring Centre for providing hour-by-hour ground-based environmental monitoring data and all PIs for their efforts in maintaining the instruments and providing data.

Conflicts of Interest: The authors declare no conflicts of interest.

References

1. Liu, H.; Liu, S.; Xue, B.; Lv, Z.; Meng, Z.; Yang, X.; Xue, T.; Yu, Q.; He, K. Ground-Level Ozone Pollution and Its Health Impacts in China. *Atmos. Environ.* **2018**, *173*, 223–230. [CrossRef]
2. Ma, X.; Huang, J.; Zhao, T.; Liu, C.; Zhao, K.; Xing, J.; Xiao, W. Rapid Increase in Summer Surface Ozone over the North China Plain during 2013–2019: A Side Effect of Particulate Matter Reduction Control? *Atmos. Chem. Phys.* **2021**, *21*, 1–16. [CrossRef]
3. Oksanen, E. Impacts of Ozone on Forest Plants and Ecosystems. *Forests* **2021**, *12*, 1345. [CrossRef]
4. Wang, Y.; Gao, W.; Wang, S.; Song, T.; Gong, Z.; Ji, D.; Wang, L.; Liu, Z.; Tang, G.; Huo, Y.; et al. Contrasting Trends of PM2.5 and Surface-Ozone Concentrations in China from 2013 to 2017. *Natl. Sci. Rev.* **2020**, *7*, 1331–1339. [CrossRef]
5. Liu, Y.; Wang, T. Worsening Urban Ozone Pollution in China from 2013 to 2017—Part 2: The Effects of Emission Changes and Implications for Multi-Pollutant Control. *Atmos. Chem. Phys.* **2020**, *20*, 6323–6337. [CrossRef]
6. Tan, Z.; Lu, K.; Hofzumahaus, A.; Fuchs, H.; Bohn, B.; Holland, F.; Liu, Y.; Rohrer, F.; Shao, M.; Sun, K.; et al. Experimental Budgets of OH, HO_2, and RO_2 Radicals and Implications for Ozone Formation in the Pearl River Delta in China 2014. *Atmos. Chem. Phys.* **2019**, *19*, 7129–7150. [CrossRef]
7. Atkinson, R. Atmospheric Chemistry of VOCs and NOx. *Atmos. Environ.* **2000**, *34*, 2063–2101. [CrossRef]
8. Hong, Q.; Liu, C.; Chan, K.L.; Hu, Q.; Xie, Z.; Liu, H.; Si, F.; Liu, J. Ship-Based MAX-DOAS Measurements of Tropospheric NO_2, SO_2, and HCHO Distribution along the Yangtze River. *Atmos. Chem. Phys.* **2018**, *18*, 5931–5951. [CrossRef]
9. Souri, A.H.; Nowlan, C.R.; Wolfe, G.M.; Lamsal, L.N.; Chan Miller, C.E.; Abad, G.G.; Janz, S.J.; Fried, A.; Blake, D.R.; Weinheimer, A.J.; et al. Revisiting the Effectiveness of HCHO/NO_2 Ratios for Inferring Ozone Sensitivity to Its Precursors Using High Resolution Airborne Remote Sensing Observations in a High Ozone Episode during the KORUS-AQ Campaign. *Atmos. Environ.* **2020**, *224*, 117341. [CrossRef]
10. Valin, L.C.; Fiore, A.M.; Chance, K.; González Abad, G. The Role of OH Production in Interpreting the Variability of CH_2O Columns in the Southeast U.S. *JGR Atmos.* **2016**, *121*, 478–493. [CrossRef]

11. Martin, R.V.; Parrish, D.D.; Ryerson, T.B.; Nicks, D.K.; Chance, K.; Kurosu, T.P.; Jacob, D.J.; Sturges, E.D.; Fried, A.; Wert, B.P. Evaluation of GOME Satellite Measurements of Tropospheric NO_2 and HCHO Using Regional Data from Aircraft Campaigns in the Southeastern United States. *J. Geophys. Res.* **2004**, *109*, D24307. [CrossRef]
12. Jin, X.; Fiore, A.; Boersma, K.F.; Smedt, I.D.; Valin, L. Inferring Changes in Summertime Surface Ozone-NO_x-VOC Chemistry over U.S. Urban Areas from Two Decades of Satellite and Ground-Based Observations. *Environ. Sci. Technol.* **2020**, *54*, 6518–6529. [CrossRef]
13. Ren, J.; Guo, F.; Xie, S. Diagnosing Ozone-NO_x-VOC Sensitivity and Revealing Causes of Ozone Increases in China Based on 2013–2021 Satellite Retrievals. *Atmos. Chem. Phys.* **2022**, *22*, 15035–15047. [CrossRef]
14. Witte, J.C.; Duncan, B.N.; Douglass, A.R.; Kurosu, T.P.; Chance, K.; Retscher, C. The Unique OMI HCHO/NO_2 Feature during the 2008 Beijing Olympics: Implications for Ozone Production Sensitivity. *Atmos. Environ.* **2011**, *45*, 3103–3111. [CrossRef]
15. Lin, H.; Xing, C.; Hong, Q.; Liu, C.; Ji, X.; Liu, T.; Lin, J.; Lu, C.; Tan, W.; Li, Q.; et al. Diagnosis of Ozone Formation Sensitivities in Different Height Layers via MAX-DOAS Observations in Guangzhou. *JGR Atmos.* **2022**, *127*, e2022JD036803. [CrossRef]
16. Xue, J.; Zhao, T.; Luo, Y.; Miao, C.; Su, P.; Liu, F.; Zhang, G.; Qin, S.; Song, Y.; Bu, N.; et al. Identification of Ozone Sensitivity for NO_2 and Secondary HCHO Based on MAX-DOAS Measurements in Northeast China. *Environ. Int.* **2022**, *160*, 107048. [CrossRef] [PubMed]
17. Chen, Y.; Wang, M.; Yao, Y.; Zeng, C.; Zhang, W.; Yan, H.; Gao, P.; Fan, L.; Ye, D. Research on the Ozone Formation Sensitivity Indicator of Four Urban Agglomerations of China Using Ozone Monitoring Instrument (OMI) Satellite Data and Ground-Based Measurements. *Sci. Total Environ.* **2023**, *869*, 161679. [CrossRef]
18. Wang, M.; Sheng, H.; Liu, Y.; Wang, G.; Huang, H.; Fan, L.; Ye, D. Research on the Diurnal Variation Characteristics of Ozone Formation Sensitivity and the Impact of Ozone Pollution Control Measures in "2 + 26" Cities of Henan Province in Summer. *Sci. Total Environ.* **2023**, *888*, 164121. [CrossRef] [PubMed]
19. Duncan, B.N.; Yoshida, Y.; Olson, J.R.; Sillman, S.; Martin, R.V.; Lamsal, L.; Hu, Y.; Pickering, K.E.; Retscher, C.; Allen, D.J.; et al. Application of OMI Observations to a Space-Based Indicator of NOx and VOC Controls on Surface Ozone Formation. *Atmos. Environ.* **2010**, *44*, 2213–2223. [CrossRef]
20. Jin, X.; Holloway, T. Spatial and Temporal Variability of Ozone Sensitivity over China Observed from the Ozone Monitoring Instrument. *JGR Atmos.* **2015**, *120*, 7229–7246. [CrossRef]
21. Curci, G.; Palmer, P.I.; Kurosu, T.P.; Chance, K.; Visconti, G. Estimating European Volatile Organic Compound Emissions Using Satellite Observations of Formaldehyde from the Ozone Monitoring Instrument. *Atmos. Chem. Phys.* **2010**, *10*, 11501–11517. [CrossRef]
22. Li, X.; Brauers, T.; Hofzumahaus, A.; Lu, K.; Li, Y.P.; Shao, M.; Wagner, T.; Wahner, A. MAX-DOAS Measurements of NO_2, HCHO and CHOCHO at a Rural Site in Southern China. *Atmos. Chem. Phys.* **2013**, *13*, 2133–2151. [CrossRef]
23. Stavrakou, T. Evaluating the Performance of Pyrogenic and Biogenic Emission Inventories against One Decade of Space-Based Formaldehyde Columns. *Atmos. Chem. Phys.* **2009**, *9*, 1037–1060. [CrossRef]
24. Kang, Y.; Tang, G.; Li, Q.; Liu, B.; Yao, D.; Wang, Y.; Wang, Y.; Wang, Y.; Liu, W. Problems with and Improvement of HCHO/NO_2 for Diagnosing Ozone Sensitivity—A Case in Beijing. *Remote Sens.* **2023**, *15*, 1982. [CrossRef]
25. Liu, J.; Li, X.; Tan, Z.; Wang, W.; Yang, Y.; Zhu, Y.; Yang, S.; Song, M.; Chen, S.; Wang, H.; et al. Assessing the Ratios of Formaldehyde and Glyoxal to NO_2 as Indicators of O_3–NO_x–VOC Sensitivity. *Environ. Sci. Technol.* **2021**, *55*, 10935–10945. [CrossRef] [PubMed]
26. Cao, H.; Fu, T.-M.; Zhang, L.; Henze, D.K.; Miller, C.C.; Lerot, C.; Abad, G.G.; De Smedt, I.; Zhang, Q.; Van Roozendael, M.; et al. Adjoint Inversion of Chinese Non-Methane Volatile Organic Compound Emissions Using Space-Based Observations of Formaldehyde and Glyoxal. *Atmos. Chem. Phys.* **2018**, *18*, 15017–15046. [CrossRef]
27. Gratsea, M.; Vrekoussis, M.; Richter, A.; Wittrock, F.; Schönhardt, A.; Burrows, J.; Kazadzis, S.; Mihalopoulos, N.; Gerasopoulos, E. Slant Column MAX-DOAS Measurements of Nitrogen Dioxide, Formaldehyde, Glyoxal and Oxygen Dimer in the Urban Environment of Athens. *Atmos. Environ.* **2016**, *135*, 118–131. [CrossRef]
28. Chen, Y.; Su, W.; Xing, C.; Yin, H.; Lin, H.; Zhang, C.; Liu, H.; Hu, Q.; Liu, C. Kilometer-Level Glyoxal Retrieval via Satellite for Anthropogenic Volatile Organic Compound Emission Source and Secondary Organic Aerosol Formation Identification. *Remote Sens. Environ.* **2022**, *270*, 112852. [CrossRef]
29. Lerot, C.; Hendrick, F.; Roozendael, M.V.; Alvarado, L.M.A.; Richter, A.; Smedt, I.D.; Theys, N.; Vlietinck, J.; Yu, H.; Gent, J.V.; et al. Glyoxal Tropospheric Column Retrievals from TROPOMI—Multi-Satellite Intercomparison and Ground-Based Validation. *Atmos. Meas. Tech.* **2021**, *14*, 7775–7807. [CrossRef]
30. Zhang, K.; Li, L.; Huang, L.; Wang, Y.; Huo, J.; Duan, Y.; Wang, Y.; Fu, Q. The Impact of Volatile Organic Compounds on Ozone Formation in the Suburban Area of Shanghai. *Atmos. Environ.* **2020**, *232*, 117511. [CrossRef]
31. Han, S.; Bian, H.; Feng, Y.; Liu, A.; Li, X.; Zeng, F.; Zhang, X. Analysis of the Relationship between O_3, NO and NO_2 in Tianjin, China. *Aerosol Air Qual. Res.* **2011**, *11*, 128–139. [CrossRef]

32. De Smedt, I.; Pinardi, G.; Vigouroux, C.; Compernolle, S.; Bais, A.; Benavent, N.; Boersma, F.; Chan, K.-L.; Donner, S.; Eichmann, K.-U.; et al. Comparative Assessment of TROPOMI and OMI Formaldehyde Observations against MAX-DOAS Network Column Measurements. *Atmos. Chem. Phys.* **2021**, *21*, 12561–12593. [CrossRef]
33. Veefkind, J.P.; Aben, I.; McMullan, K.; Förster, H.; De Vries, J.; Otter, G.; Claas, J.; Eskes, H.J.; De Haan, J.F.; Kleipool, Q.; et al. TROPOMI on the ESA Sentinel-5 Precursor: A GMES Mission for Global Observations of the Atmospheric Composition for Climate, Air Quality and Ozone Layer Applications. *Remote Sens. Environ.* **2012**, *120*, 70–83. [CrossRef]
34. Liu, S.; Valks, P.; Pinardi, G.; Xu, J.; Chan, K.L.; Argyrouli, A.; Lutz, R.; Beirle, S.; Khorsandi, E.; Baier, F.; et al. An Improved TROPOMI Tropospheric NO_2 Research Product over Europe. *Atmos. Meas. Tech.* **2021**, *14*, 7297–7327. [CrossRef]
35. De Smedt, I.; Theys, N.; Yu, H.; Danckaert, T.; Lerot, C.; Compernolle, S.; Van Roozendael, M.; Richter, A.; Hilboll, A.; Peters, E.; et al. Algorithm Theoretical Baseline for Formaldehyde Retrievals from S5P TROPOMI and from the QA4ECV Project. *Atmos. Meas. Tech.* **2018**, *11*, 2395–2426. [CrossRef]
36. Vigouroux, C.; Langerock, B.; Bauer Aquino, C.A.; Blumenstock, T.; Cheng, Z.; De Mazière, M.; De Smedt, I.; Grutter, M.; Hannigan, J.W.; Jones, N.; et al. TROPOMI–Sentinel-5 Precursor Formaldehyde Validation Using an Extensive Network of Ground-Based Fourier-Transform Infrared Stations. *Atmos. Meas. Tech.* **2020**, *13*, 3751–3767. [CrossRef]
37. Li, Y.; Yu, C.; Tao, J.; Lu, X.; Chen, L. Analysis of Ozone Formation Sensitivity in Chinese Representative Regions Using Satellite and Ground-Based Data. *Remote Sens.* **2024**, *16*, 316. [CrossRef]
38. Li, R.; Xu, M.; Li, M.; Chen, Z.; Zhao, N.; Gao, B.; Yao, Q. Identifying the Spatiotemporal Variations in Ozone Formation Regimes across China from 2005 to 2019 Based on Polynomial Simulation and Causality Analysis. *Atmos. Chem. Phys.* **2021**, *21*, 15631–15646. [CrossRef]
39. Pusede, S.E.; Cohen, R.C. On the Observed Response of Ozone to NO_x and VOC Reactivity Reductions in San Joaquin Valley California 1995–Present. *Atmos. Chem. Phys.* **2012**, *12*, 8323–8339. [CrossRef]
40. Sillman, S. The Relation between Ozone, NOx and Hydrocarbons in Urban and Polluted Rural Environments. *Atmos. Environ.* **1999**, *33*, 1821–1845. [CrossRef]
41. Kleinman, L.I. Low and High NO_x Tropospheric Photochemistry. *J. Geophys. Res.* **1994**, *99*, 16831–16838. [CrossRef]
42. Schroeder, J.R.; Crawford, J.H.; Fried, A.; Walega, J.; Weinheimer, A.; Wisthaler, A.; Müller, M.; Mikoviny, T.; Chen, G.; Shook, M.; et al. New Insights into the Column CH_2O/NO_2 Ratio as an Indicator of Near-surface Ozone Sensitivity. *JGR Atmos.* **2017**, *122*, 8885–8907. [CrossRef]
43. Jin, X.; Fiore, A.M.; Murray, L.T.; Valin, L.C.; Lamsal, L.N.; Duncan, B.; Folkert Boersma, K.; De Smedt, I.; Abad, G.G.; Chance, K.; et al. Evaluating a Space-Based Indicator of Surface Ozone-NO_x-VOC Sensitivity Over Midlatitude Source Regions and Application to Decadal Trends. *JGR Atmos.* **2017**, *122*, 10439–10461. [CrossRef]
44. Li, L.; Xie, F.; Li, J.; Gong, K.; Xie, X.; Qin, Y.; Qin, M.; Hu, J. Diagnostic Analysis of Regional Ozone Pollution in Yangtze River Delta, China: A Case Study in Summer 2020. *Sci. Total Environ.* **2022**, *812*, 151511. [CrossRef]
45. Liu, Z.; Hu, K.; Zhang, K.; Zhu, S.; Wang, M.; Li, L. VOCs Sources and Roles in O_3 Formation in the Central Yangtze River Delta Region of China. *Atmos. Environ.* **2023**, *302*, 119755. [CrossRef]
46. Zhao, M.; Zhang, Y.; Pei, C.; Chen, T.; Mu, J.; Liu, Y.; Wang, Y.; Wang, W.; Xue, L. Worsening Ozone Air Pollution with Reduced NO and VOCs in the Pearl River Delta Region in Autumn 2019: Implications for National Control Policy in China. *J. Environ. Manag.* **2022**, *324*, 116327. [CrossRef] [PubMed]
47. Wang, X.; Yin, S.; Zhang, R.; Yuan, M.; Ying, Q. Assessment of Summertime O_3 Formation and the O_3-NO_X-VOC Sensitivity in Zhengzhou, China Using an Observation-Based Model. *Sci. Total Environ.* **2022**, *813*, 152449. [CrossRef] [PubMed]
48. Wang, R.; Wang, L.; Sun, J.; Zhang, L.; Li, Y.; Li, K.; Liu, B.; Zhang, J.; Wang, Y. Maximizing Ozone Control by Spatial Sensitivity-Oriented Mitigation Strategy in the Pearl River Delta Region, China. *Sci. Total Environ.* **2023**, *905*, 166987. [CrossRef]
49. Wang, J.; Zhang, Y.; Xiao, S.; Wu, Z.; Wang, X. Ozone Formation at a Suburban Site in the Pearl River Delta Region, China: Role of Biogenic Volatile Organic Compounds. *Atmosphere* **2023**, *14*, 609. [CrossRef]
50. Zeng, L.; Yang, J.; Guo, H.; Lyu, X. Impact of NOx Reduction on Long-Term Surface Ozone Pollution in Roadside and Suburban Hong Kong: Field Measurements and Model Simulations. *Chemosphere* **2022**, *302*, 134816. [CrossRef]
51. Wang, N.; Du, Y.; Chen, D.; Meng, H.; Chen, X.; Zhou, L.; Shi, G.; Zhan, Y.; Feng, M.; Li, W.; et al. Spatial Disparities of Ozone Pollution in the Sichuan Basin Spurred by Extreme, Hot Weather. *Atmos. Chem. Phys.* **2024**, *24*, 3029–3042. [CrossRef]
52. Wang, D.; Zhou, J.; Han, L.; Tian, W.; Wang, C.; Li, Y.; Chen, J. Source Apportionment of VOCs and Ozone Formation Potential and Transport in Chengdu, China. *Atmos. Pollut. Res.* **2023**, *14*, 101730. [CrossRef]
53. Guan, Y.; Liu, X.; Zheng, Z.; Dai, Y.; Du, G.; Han, J.; Hou, L.; Duan, E. Summer O_3 Pollution Cycle Characteristics and VOCs Sources in a Central City of Beijing-Tianjin-Hebei Area, China. *Environ. Pollut.* **2023**, *323*, 121293. [CrossRef]
54. Zhang, H.; Li, A.; Hu, Z.; Ren, H.; Zhong, H.; Guo, J.; Yun, L.; Zhang, M. Observation on the Aerosol and Ozone Precursors in Suburban Areas of Shenzhen and Analysis of Potential Source Based on MAX-DOAS. *J. Environ. Sci.* **2023**, *132*, 109–121. [CrossRef]

55. Li, C.; Wang, H.; Chen, X.; Zhai, T.; Ma, X.; Yang, X.; Chen, S.; Li, X.; Zeng, L.; Lu, K. Observation and Modeling of Organic Nitrates on a Suburban Site in Southwest China. *Sci. Total Environ.* **2023**, *859*, 160287. [CrossRef]
56. Rappenglück, B.; Dasgupta, P.K.; Leuchner, M.; Li, Q.; Luke, W. Formaldehyde and Its Relation to CO, PAN, and SO_2 in the Houston-Galveston Airshed. *Atmos. Chem. Phys.* **2010**, *10*, 2413–2424. [CrossRef]
57. Parrish, D.D.; Ryerson, T.B.; Mellqvist, J.; Johansson, J.; Fried, A.; Richter, D.; Walega, J.G.; Washenfelder, R.A.; De Gouw, J.A.; Peischl, J.; et al. Primary and Secondary Sources of Formaldehyde in Urban Atmospheres: Houston Texas Region. *Atmos. Chem. Phys.* **2012**, *12*, 3273–3288. [CrossRef]
58. Li, L.Y.; Chen, Y.; Xie, S.D. Spatio-Temporal Variation of Biogenic Volatile Organic Compounds Emissions in China. *Environ. Pollut.* **2013**, *182*, 157–168. [CrossRef] [PubMed]
59. Fu, T.; Jacob, D.J.; Wittrock, F.; Burrows, J.P.; Vrekoussis, M.; Henze, D.K. Global Budgets of Atmospheric Glyoxal and Methylglyoxal, and Implications for Formation of Secondary Organic Aerosols. *J. Geophys. Res.* **2008**, *113*, D15303. [CrossRef]
60. Kaiser, J.; Wolfe, G.M.; Min, K.E.; Brown, S.S.; Miller, C.C.; Jacob, D.J.; deGouw, J.A.; Graus, M.; Hanisco, T.F.; Holloway, J.; et al. Reassessing the Ratio of Glyoxal to Formaldehyde as an Indicator of Hydrocarbon Precursor Speciation. *Atmos. Chem. Phys.* **2015**, *15*, 7571–7583. [CrossRef]
61. Chan Miller, C.; Jacob, D.J.; Marais, E.A.; Yu, K.; Travis, K.R.; Kim, P.S.; Fisher, J.A.; Zhu, L.; Wolfe, G.M.; Hanisco, T.F.; et al. Glyoxal Yield from Isoprene Oxidation and Relation to Formaldehyde: Chemical Mechanism, Constraints from SENEX Aircraft Observations, and Interpretation of OMI Satellite Data. *Atmos. Chem. Phys.* **2017**, *17*, 8725–8738. [CrossRef]
62. Singh, A.; Ring, A.M.; He, H.; Allen, D.J.; Dickerson, R.R.; Salawitch, R.J.; Canty, T.P. Inferring Near-Surface Ozone Production Regimes: Insights from Using Satellite Retrievals over the Contiguous US. *Atmos. Environ.* **2025**, *352*, 121208. [CrossRef]
63. Ryan, R.G.; Rhodes, S.; Tully, M.; Schofield, R. Surface Ozone Exceedances in Melbourne, Australia Are Shown to Be under NOx Control, as Demonstrated Using Formaldehyde:NO_2 and Glyoxal:Formaldehyde Ratios. *Sci. Total Environ.* **2020**, *749*, 141460. [CrossRef] [PubMed]

Disclaimer/Publisher's Note: The statements, opinions and data contained in all publications are solely those of the individual author(s) and contributor(s) and not of MDPI and/or the editor(s). MDPI and/or the editor(s) disclaim responsibility for any injury to people or property resulting from any ideas, methods, instructions or products referred to in the content.